Structure and proton conduction in sulfonated poly(ether ether ketone) semi-permeable membranes: a multi-scale computational approach

Journal:	*Physical Chemistry Chemical Physics*
Manuscript ID	CP-ART-01-2019-000598.R1
Article Type:	Paper
Date Submitted by the Author:	21-Mar-2019
Complete List of Authors:	Molina, Jarol; Corporacion Universitaria Minuto de Dios - UNIMINUTO, Departamento de Ciencias Basicas de Pablo, Juan J.; Liew Family Professor of Molecular Theory and Simulation, Institute for Molecular Engineering Hernandez-Ortiz, Juan; Universidad Nacional de Colombia, Sede Medellinin, Department of Materials and Nanotechnology; University of Chicago, Institute for Molecular Engineering

Journal Name

ARTICLE TYPE

Cite this: DOI: 10.1039/xxxxxxxxxx

Structure and proton conduction in sulfonated poly(ether ether ketone) semi-permeable membranes: a multi-scale computational approach

Jarol Molina,[a] Juan de Pablo,[b,c] and Juan P. Hernández-Ortiz[d,e*]

Received Date
Accepted Date

DOI: 10.1039/xxxxxxxxxx

www.rsc.org/journalname

The design of polymeric membranes for proton or ionic exchange highly depends on the fundamental understanding of the physical and molecular mechanisms that control the formation of the conduction channels. There is an inherent relation between the dynamical structure of the polymeric membrane and the electrostatic forces that drive membrane segregation and proton transport. Here, we used a multi-scale computational approach to analyze the morphology of sulfonated poly(ether ether ketone) membranes at the mesoscale. A self-consistent description of the electrostatic phenomenon was adopted, where discrete polymer chains and a continuum proton field were embedded in a continuum fluid. Brownian dynamics was used for the evolution of the suspended polymer molecules, while a convection–diffusion transport equation, including the Nernst-Planck diffusion mechanism, accounted for the dynamics of the proton concentration field. We varied the polymer concentration, the degree of sulfonation and the level of confinement to find relationships between membrane structure and proton conduction. Our results indicate that the reduced mobility of polymer chains, at concentrations above overlap, and a moderate degree of sulfonation – i.e., 30% – are essential elements for membrane segregation and proton domain connectivity. These conditions also ensure that the membrane structure is not affected by size or by potential gradients. Importantly, our analysis shows that membrane conductivity and current are linearly dependent on polymer concentration and quadratically dependent on the degree of sulfonation. We found that the optimal polymeric membrane design requires a polymer concentration above overlap and a degree of sulfonation around 50%. These conditions promote a dynamical membrane morphology with a constant density of proton channels. Our results and measurements agree with previous experimental works, thereby validating our model and observations.

1 Introduction

The selective transport of chemical species through membranes is central in many biological and technological systems[1–5]. The characteristics of the structural membrane component determine the conditions and forces that control the dynamic morphology of the membrane and the formation of the transport channels. From the technological perspective, a comprehensive understanding of the molecular interplay between the membrane components and the transported species is vital to mimic biological systems in engineering and physics. For instance, polyelectrolyte membranes have received a lot of attention in the last decade due to their capacity to perform selective transport for fuel cell applications. These alternative energetic platforms offer numerous potential benefits, such as high efficiency, high power density, low or zero emissions and reliability.

Polymeric proton exchange membranes, typically used in polymer membrane fuel cells and in direct methanol fuel cells, foster proper transport environments for proton conduction from the anode to the cathode. They provide selective barriers against electrons, gas and fuel molecules. Among the portfolio of polymers, previous efforts have shown that sulfonated poly(ether ether ketone) (SPEEK), see Fig. 1A, is a promising option for fuel cell application as it possesses good thermal stability, mechanical strength and adequate proton conductivity. SPEEK is a sulfonated

[a] Departamento de Ciencias Básicas, Corporación Universitaria Minuto de Dios - UNIMINUTO, Bello, Antioquia, Colombia.
[b] Institute for Molecular Engineering, University of Chicago, Chicago, IL 60637.
[c] Materials Science Division, Argonne National Laboratory, Lemont, IL 60439.
[d] Departamento de Materiales y Nanotecnología, Universidad Nacional de Colombia–Medellín, Medellín Colombia.
[e] Colombia/Wisconsin One-Health Consortium, Universidad Nacional de Colombia–Medellín, Medellín Colombia.
* Corresponding author E-mail: jphernandezo@unal.edu.co; jphernandezo@wisc.edu

hydrocarbon polymer and it stands as a hydrophobic–hydrophilic polymer that promotes segregation and the formation of highly branched, narrow channels for proton conduction. The presence of the sulfonic acid (R-SO_3H) in the monomers determines the polarity of the polymer segments, i.e. unsulfonated monomers are hydrophobic, while sulfonated ones are hydrophilic. Therefore, the fraction of sulfonated monomers, or the degree of sulfonation (DS), determines the charge and the level of amphiphilicity of the polymer molecule. Typical SPEEK membranes employed in fuel cells contain a DS between 15% and 50%, which, in the context of Fig. 1A, is defined by:

$$\mathrm{DS} = \frac{\mathrm{ns}}{\mathrm{n}+\mathrm{ns}}. \tag{1}$$

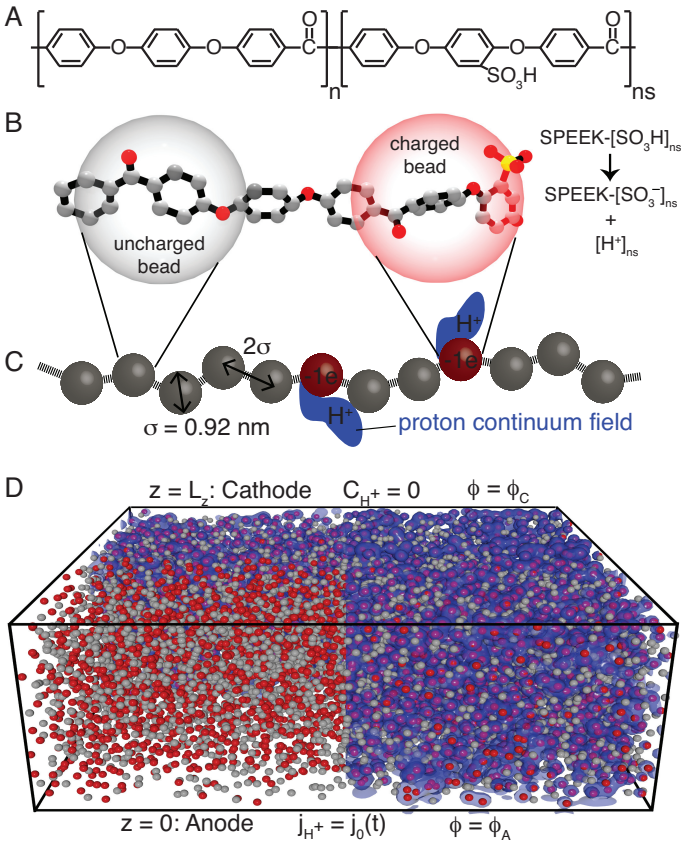

Fig. 1 A. Sulfonated poly(ether ether ketone) monomeric structures; **B.** Coarse-grain representation of the Kuhn segment and SO_3H group depronotation; **C.** SPEEK bead-spring model; and **D.** Schematic of the semi-permeable membrane.

The polymer volume fraction, Φ_P, in a semi-permeable membrane is always above polymer overlap ($\Phi_P > \Phi_{P,\mathrm{OL}} = 0.6$), the water content is low and the concentration of protons is related to the degree of sulfonation: the SO_3H groups are deprotonated resulting in SO_3^- + H^+ (Fig. 1B). Consequently, the SPEEK monomers that hold the sulfonic acids become negatively charged and the water solvent receives the protons, thereby acquiring a positive charge. Recall that the principal characteristic of a polymeric membrane for proton exchange is the species' selectivity. Low efficiency in fuel cells and energy losses are associated to poorly selective membranes[6]. Therefore, a fundamental understanding of the molecular forces that control and relate membrane structure with proton conduction is central in the design of these systems, which motivated previous theoretical efforts[7–10]. In a semi-permeable polymeric membrane, rapid dynamics, such as the diffusion of protons, molecular vibrations and water transport, are coupled to slower processes, such as the diffusion of the long polymer chains; thus, the difference between characteristic time scales range from three to ten orders of magnitude. These restrictions forced past works to rely in simulations over atomistic scales[11,12], mesoscopic scales ignoring electrostatic interactions[9,13] or discrete models with simplified electrostatic considerations[14–16].

Motivated by the intrinsic relation between the polymer chemical characteristics, the membrane segregation and proton conduction, we resort to a multi-scale computational approach to model a semi-permeable SPEEK membrane at the mesoscale. The highly concentrated polyelectrolyte molecules are suspended in a continuum solvent harboring protons. Importantly, we use a continuum concentration field for the protons, which parallels stochastic approaches that use continuum approximations to model the momentum transfer for the "small" molecules. Our objective is to provide novel insights about the membrane structure and to predict the formation of conduction channels over tens or hundreds of nanometers.

We start this manuscript with the mathematical description of the polymeric membrane, the evolution equations and the required variation of the General geometry Ewald-like method (GgEm)[17,18] needed to properly calculate the electrostatic contributions. We then proceed to describe the results for the polyelectrolyte membranes, where polymer concentration, confinement and degree of sulfonation are varied. We make conclusions regarding the limiting conditions for membrane stability, we estimate membrane conductivity and current and, lastly, we summarize our most important conclusions.

2 Model and Mathematical Method

2.1 Polymer model

SPEEK is a flexible molecule with a Kuhn segment (b) that spans approximately three aromatic rings[19–22] (Fig. 1A-B). We use a bead-spring model to represent the polymer molecule, where each bead covers the volume of three aromatic rings, resulting in a bead diameter $\sigma = 0.92$ nm.

The N beads that form a polymer molecule are connected with finitely extensible non-linear elastic springs with a non-zero equilibrium distance, i.e., a FENE-Fraenkel (FF) spring[23] (Fig. 1C). The elastic force between two interconnecting beads ν and μ is then defined as follows:

$$\mathbf{f}^{\mathrm{S}}_{\nu\mu}(\mathbf{r}_{\nu\mu}) = H\mathbf{Q}\frac{1-q/|\mathbf{Q}|}{1-[(|\mathbf{Q}|-q)(q_{\max}-q)]^2}, \tag{2}$$

where H is the spring constant, $\mathbf{Q} = \mathbf{x}_\mu - \mathbf{x}_\nu$ is the connector vector between the beads, q is the non-zero equilibrium length and $q_{\max}$ is the spring maximum extension. In particular, we use $H = 100k_BT$, $q = 2\sigma = 1.84$ nm and $q_{\max} = 3.7\sigma = 3.4$ nm.

A bead-spring representation of the SPEEK polymer with a contour length $L = 337$ nm requires $N = 100$ monomers. It corresponds to a molecular weight of 2.67×10^4 g/mol. Past experimental work places the average polymer molecular weight around 3.92×10^4 g/mol[24]. We adopt the Gaussian radius of gyration, $R_G = b^2N/6 = 3.76$ nm, as the characteristic size for the polymer molecule that will help us identify the polymer concentration and the level of confinement during the simulations.

The polymer model includes additional bead-to-bead and bead-to-wall excluded volume interactions, where a repulsive Lennard-Jones or Weeks-Chandler-Andersen (WCA) potential[25,26] is used with a characteristic energy scale given by $\varepsilon = k_BT$, i.e.,

$$\phi_{\nu\mu}^{\mathrm{WCA}} = 4\varepsilon\left[\left(\frac{\sigma}{r_{\nu\mu}}\right)^{12} - \left(\frac{\sigma}{r_{\nu\mu}}\right)^{6}\right] + \varepsilon, \tag{3}$$

if the distance between the beads $r_{\nu\mu} = |\mathbf{x}_\mu - \mathbf{x}_\nu| \leq 2^{1/6}\sigma$, while $\phi_{\nu\mu}^{\mathrm{WCA}} = 0$ for $r_{\nu\mu} > 2^{1/6}\sigma$.

2.2 Membrane

The semi-permeable membrane is constructed by confining the polymer molecules in a slit geometry $L_x \times L_y \times L_z$ (Fig. 1D). The system is considered periodic in the $xy-$plane. The level of confinement and the size of the membrane are determined by the molecule radius of gyration. In particular, we use $L_z = [5R_G, 10R_G]$. The periodic dimensions are $L_x = L_y = 3L_z$, ensuring that the electrostatic interactions are not affected by the periodic images[17,27–29]. The polymer concentration is varied and measured with the polymer volume fraction that is defined as follows:

$$\Phi_P = \frac{\left[N_P\left(4/3\pi R_G^3\right)\right]}{\left[9L_z^3\right]}, \tag{4}$$

where N_P is the number of polymer molecules. Here, we consider three concentration regimens, namely finite-concentration, overlap and concentrated, i.e., $\Phi_P = [0.4, 0.6, 0.8]$, respectively. For completeness, these regimens required simulations with 75 to 2,000 polymer chains and up to 200,000 monomer beads. The hydrated membrane density for $\Phi_P = [0.4, 0.6, 0.8]$ are 7.98×10^4 g/mol, 1.19×10^5 g/mol and 1.59×10^5 g/mol, respectively.

The nature of the polymer charge is the de-protonation of the sulfonic acids (Fig. 1B). Therefore, the total proton concentration is calculated according to the degree of sulfonation (DS):

$$C_+^0 = \frac{N_P}{9L_z^3N_A}\mathrm{DS}, \tag{5}$$

where N_A is Avogadro's number. During our simulations, the number of polymer molecules remain constant; therefore, the total proton concentration, C_+^0, is also kept constant to ensure global electro-neutrality.

We denote $z = 0$ as the anode and $z = L_z$ as the cathode. In the anode, we impose a known proton flux condition, $\mathbf{j}_+(z=0) = \mathbf{j}_0$, considering that it is the place where the fuel decomposition reaction occurs. The flux is calculated every time to ensure that C_+^0 is constant. On the other hand, at the cathode, we assume an instantaneous reaction, represented by a homogenous Dirichlet boundary condition for the proton concentration: $C_+(z = L_z) = 0$. The electrostatic potential at both, anode (ϕ_A) and cathode (ϕ_C), are known, thereby representing conducting walls.

2.3 Evolution equations

The stochastic differential equation that governs the dynamics of the polymer beads in a viscous solvent is obtained from the force balance on each bead. Neglecting inertia – the Reynolds number is zero – we write

$$\mathbf{f}_\nu^h + \mathbf{f}_\nu^B + \mathbf{f}_\nu^S + \mathbf{f}_\nu^E + \mathbf{f}_\nu^v + \mathbf{f}_\nu^w = 0, \tag{6}$$

for each bead $\nu = 1, ..., N\times N_P$, where, $\mathbf{f}_\nu^h$ is the hydrodynamic force, $\mathbf{f}_\nu^B$ is the Brownian force, $\mathbf{f}_\nu^S$ is any configurational spring force, $\mathbf{f}_\nu^v$ is the bead-bead excluded volume, $\mathbf{f}_\nu^w$ is the wall-bead excluded volume and $\mathbf{f}_\nu^E$ is the electrostatic force.

The diffusion equation for the probability distribution function for the bead locations has the form of a Fokker-Planck equation, which is equivalently represented by an stochastic differential equation for the evolution of the bead positions:[30,31]

$$d\mathbf{R} = \left[\mathbf{U}_0 + \mathbf{M}\cdot\mathbf{F} + \frac{\partial}{\partial\mathbf{x}}\cdot\mathbf{D}\right]dt + \sqrt{2}\mathbf{B}\cdot d\mathbf{W}, \tag{7}$$

where $\mathbf{R} = (\mathbf{x}_1, \mathbf{x}_2, ..., \mathbf{x}_{N\times N_P})$ is a $3N\times N_P$ vector containing the spatial coordinates of the beads, $\mathbf{U}_0$ denotes a $3N\times N_P$ vector with the unperturbed fluid velocity at the bead's position, $\mathbf{D} = k_BT\mathbf{M}$ is the $[3N\times N_P]\times[3N\times N_P]$ diffusion tensor, $\mathbf{F}$ is a $3N\times N_P$ vector with the non-Brownian and non-hydrodynamic components of the force, k_B is Boltzmann's constant and $T = 298$ K is the temperature. The diffusion tensor is given by $\mathbf{D} = k_BT\mathbf{M}$, where $\mathbf{M}$ is the mobility tensor that includes the Stokes' drag and the pairwise Stokeslets that account for the hydrodynamic interactions between beads[18,32–34]. In this work, we ignore these interactions accounting that the systems are highly confined. Consequently, the diffusion tensor is reduced to a constant diagonal tensor and the drift term, $\partial/\partial\mathbf{x}\cdot\mathbf{D}$, is zero. Finally, $d\mathbf{W}$ is a random vector, the components of which are obtained from a real-valued Gaussian distribution with zero mean and variance dt. It is coupled with the diffusion tensor through the fluctuation-dissipation theorem: $\mathbf{D} = \mathbf{B}\cdot\mathbf{B}^T$.

The dynamics of the proton concentration field, $C_+(\mathbf{x})$, is obtained from a species mass balance, resulting in a convection-diffusion equation:

$$\frac{\partial C_+}{\partial t} = -\nabla\cdot\mathbf{j}_+. \tag{8}$$

Ignoring fluctuating hydrodynamic velocities, the diffusive flux, $\mathbf{j}_+$, is given by the Nernst-Planck expression[17,35,36]:

$$\mathbf{j}_+ = -D\left[\nabla C_+ + \left(\frac{q_+}{k_BT}\right)C_+\nabla\phi\right], \tag{9}$$

where $D = 2.26\times10^{-5}$ cm^2/s[37,38] is the diffusion coefficient of the protons and $q_+ = +e$ the elementary charge. The characteristic time for the continuum ions to diffuse over the polymer bead is $\sigma^2/D \approx 3.8^{-10}$ s, while the bead diffusion time is $\zeta\sigma^2/k_BT \approx 2\times10^{-7}$ s. These times provide the numerical resolution of the time stepping, i.e. they are the smallest time scale

to be resolved. In addition, the polymer diffusion time over the membrane thickness determines how long the simulation must be carried out to ensure good statistics. Our simulations were run over 20 to 50 membrane diffusion times (around 10^{-2} s).

2.4 Electrostatic forces and the NP-GgEm

The charged polymer beads and the protons contribute to the charge density, $\rho(\mathbf{x})$. As the charges diffuse, local electroneutrality is not satisfied and the charge density drives an electrostatic potential given by the solution of Poisson's equation,

$$\nabla^2\phi(\mathbf{x}) = -\frac{\rho(\mathbf{x})}{\varepsilon_0\varepsilon}, \tag{10}$$

where ε_0 is the vacuum permittivity and ε is the solvent relative permittivity.

The electric field, $\mathbf{E}(\mathbf{x}) = -\nabla\phi(\mathbf{x})$, imposes an electric force, $\mathbf{f}^E$, on all the charged entities (discrete and continuum). To correctly solve Poisson's equation, appropriate boundary conditions are in order. In correspondence with the physical system that we are modeling, periodic boundary conditions are selected for the $xy-$plane, while Direchlet conditions are imposed at the confining walls, i.e. $\phi(z=0)=\phi_A$ and $\phi(z=L_z)=\phi_C$.

The polymer beads are considered "regularized" point-forces, where the charge is distributed through a Gaussian function with a variance related to their diameter σ. Consequently, the discrete beads and the continuum proton field define the following charge density:

$$\rho(\mathbf{x}) = \sum_{\nu=1}^{N\times N_P} q_P S_E(\mathbf{x}-\mathbf{x}_\nu) + N_A q_+ C_+(\mathbf{x}), \tag{11}$$

where N_A is Avogadro's number, $q_P = -1e$ is the charge of the polymer bead and $q_+ = +1e$ is the proton charge. The regularizing Gaussian function is given by:

$$S_E(\mathbf{x}) = \frac{\xi^3}{\pi^{3/2}}\exp(-\xi^2|\mathbf{x}|^2), \tag{12}$$

where ξ is the parameter that is adjusted to distribute the charge over the bead size.

The long-range nature of electrostatic forces had motivated mathematical approaches that allow the calculation of the electrostatic potential and the electric field in a fast and reliable way. Most of them are based on the Ewald summation concept for singular Green's functions[25,26,39], where the long-range $(1/r)$ decaying operator is split into fast decaying functions in real and Fourier spaces. Ewald summation methods had evolved into $O(N)$ algorithms[40–42] to treat electrostatics in free-space and periodic domains, which have already been embedded into popular molecular dynamics packages, like Gromacs[43,44] and Lammps[45]. The General geometry Ewald-like method (GgEm), developed by Hernández-Ortiz, de Pablo and Graham[18], is among those methods, having a unique feature of calculating Green's functions in any geometry; i.e., it deals with any type of boundary conditions. GgEm also offers the possibility of including another type of Green's function-based singularities, long-range interactions and fields, such as hydrodynamic interactions[46–49] and the concentration of charged continuum species (Nernst-Planck-GgEm)[17]. Details of the GgEm, including its implementation and algorithms, can be found in some of our previous works[50–53].

For completeness, the GgEm starts with redefining the charge density $\rho(\mathbf{x}) = \rho_l(\mathbf{x}) + \rho_g(\mathbf{x})$. Given the linearity of Poisson's equation, it results in a "local" and a "global" contribution of the electrostatic potential: $\phi(\mathbf{x}) = \phi_l(\mathbf{x}) + \phi_g(\mathbf{x})$. The idea is to use a smoothing function, $g_E(\alpha,\mathbf{x})$, that "screens" the local contribution over a distance of $1/\alpha$. This function must satisfy the condition $\int_{\text{all space}} g_E(\alpha,\mathbf{x})d\mathbf{x} = 1$. The most common selection for g_E is a Gaussian function[25,26]

$$g_E(\alpha,\mathbf{x}) = \frac{\alpha^3}{\pi^{3/2}}\exp(-\alpha^2|\mathbf{x}|^2). \tag{13}$$

With the inclusion of the screening function, the local charge density is written as follows:

$$\rho_l(\mathbf{x}) = \sum_{\nu=1}^{N\times N_P} q_P\left[S_E(\mathbf{x}-\mathbf{x}_\nu) - g_E(\alpha,\mathbf{x}-\mathbf{x}_\nu)\right], \tag{14}$$

while the global charge density is defined by:

$$\rho_g(\mathbf{x}) = \sum_{\nu=1}^{N\times N_P} q_P\left[g_E(\alpha,\mathbf{x}-\mathbf{x}_\nu)\right] + N_A q_+ C_+(\mathbf{x}). \tag{15}$$

The local contribution for the electrostatic potential is resolved analytically ignoring the walls. This calculation resembles a free-space Green's function calculation, i.e.

$$\phi_l(\mathbf{x}) = \sum_{\nu=1}^{N_D} q_P G_l^R(\mathbf{x}-\mathbf{x}_\nu), \tag{16}$$

where

$$G_l^R(\mathbf{x}) = \frac{1}{4\pi\varepsilon_0\varepsilon}\left[\frac{\text{erf}(\xi|\mathbf{x}|)}{|\mathbf{x}|} - \frac{\text{erf}(\alpha|\mathbf{x}|)}{|\mathbf{x}|}\right]. \tag{17}$$

On the other hand, the global contribution is approximated numerically over a mesh, with any preferred method, and using superposition between the local and global fields to impose the appropriate boundary conditions. For instance, homogeneous Dirichlet boundary conditions are obtained with $\phi_g|_{\text{wall}} = -\phi_l|_{\text{wall}}$. Particularly in this paper, we used a combination between a discrete fast Fourier transform, in the periodic directions, and finite differences in the confined direction, to resolve the global field. We included a detailed description of the numerical method in the Appendix.

The characteristic variables for the system are set by the polymer bead radius, $a = \sigma/2$, for length, bead diffusion time, $\zeta a^2/k_BT$, for time (where $\zeta = 6\pi\eta a$ is the drag coefficient and η the solvent viscosity), $e/4\pi\varepsilon_0\varepsilon a$ for the electrostatic potential, and the elementary charge e for the charge. The total concentration for the protons, C_+^0, is used as the characteristic concentration for the continuum proton field. The parameter $\beta_k = \zeta D/k_BT$ defines the ratio between the polymer bead and the proton diffusion coefficients. The ratio between electrostatic forces and thermal forces denotes the Bjerrum length, $\lambda_B = e^2/4\pi\varepsilon_0\varepsilon k_BT$, while the ionic strength, $I = {}^1\!/\!_2 C_+^0 z_+^2$, determines the Debye length, $\lambda_D^{-2} = 2N_a e^2 I/\varepsilon_0\varepsilon k_BT$.

3 Results

To best illustrate the relation between the morphology of the polymer membrane and the proton conduction, we explore how polymer concentration, confinement and electrostatic potential gradient influence the inner structure of the membrane. Our task is to lay down the basics behind the polymer–proton interactions to then proceed to study conduction channels and properties. The first questions to ask are how the protons and polymers are distributed across the membrane and how stable is the membrane.

To quantify average concentrations and distributions, we define time and ensamble averages in the z-direction and the $xz-$plane as follows:

$$\bar{\omega}(z) = \frac{1}{L_x L_y} \langle \int_0^{L_x} \int_0^{L_y} \omega(x,y,z) dx dy \rangle, \qquad (18)$$
$$\bar{\omega}(x,z) = \frac{1}{L_y} \langle \int_0^{L_y} \omega(x,y,z) dx \rangle,$$

where $\omega(x,y,z)$ is any property or measurement and $\langle\rangle$ denotes time averaging.

3.1 Internal distributions with $L_z = 5R_G$ and $\Delta\phi = 0$.

Let's begin by analyzing the time averaged distributions of protons and monomers of a membrane with $L_z = 5R_G$ containing polymers with DS $= [0.1, 0.3, 0.5]$ and in the absence of electrostatic potential differences: $\phi_A = \phi_C = 0$. Table 1 lists the proton concentrations and the corresponding Debye lengths for the $L_z = 5R_G$ membrane.

Table 1 Proton concentration and Debye lengths.

DS ↓	$\Phi_P \rightarrow$	0.4	0.6	0.8
DS = 0.1	C_+^0 (M)	0.030	0.045	0.060
	λ_D (nm)	2.50	2.05	1.77
	λ_D/σ	2.71	2.22	1.93
DS = 0.3	C_+^0 (M)	0.090	0.135	0.180
	λ_D (nm)	1.44	1.18	1.02
	λ_D/σ	1.57	1.28	1.11
DS = 0.5	C_+^0 (M)	0.151	0.255	0.299
	λ_D (nm)	1.12	0.91	0.79
	λ_D/σ	1.21	0.91	0.86

Figure 2 shows the time averaged proton concentration and number density of sulfonated and uncharged monomers as a function of the $z-$direction. The results we are presenting here are for simulations that were equilibrated between 100 and 200 polymer diffusion times over L_z (6 ms for the smaller system and 48 ms for the bigger one). The proton concentration profiles, Fig. 2(left), satisfy the anode and cathode boundary conditions, where there is a constant flux of protons at $z = 0$ and a fast reaction at $z = L_z$. A common feature between the proton profiles, despite polymer concentration and degree of sulfunation, is the presence of a local minima at $z \approx 0.8\sigma$. After the local minima, there is a natural increase in proton concentration as z approaches the center of the membrane; and, finally, there is a transition in the concentration profile, near the cathode, to accommodate the $C_+ = 0$ at $z = L_z$. Importantly, an uniform internal proton concentration is observed for $\Phi_P = 0.6$ or 0.8 at DS = 0.3, and at any polymer concentration for DS = 0.5. Conversely, an internal uniform proton concentration can never be achieved for DS = 0.1.

The time averaged number density of sulfonated $\bar{n}_S(z)$, and uncharged monomers $\bar{n}(z)$, in Fig. 2(center) and 2(right) are highly correlated with the proton concentrations. The number density for both types of monomers is zero at the walls due to the excluded volume interactions. Also, high degrees of polymer concentration and sulfonation ensure uniform internal distributions for the charged and uncharged monomers. In addition, as the polymer concentration increases, there is a layering effect of monomers near the walls, which follow previous theoretical results on confined polymer solutions and colloids[46,54–57]. However, near the anode $z = 0$, the location of the first peak in the number density of sulfonated monomers is at $z \approx 1.6\sigma$. Note that the depletion layer for $z = L_z$ is 1σ, corresponding to the excluded volume range. The location of this peak at $z \approx 1.6\sigma$ is due to the electrostatic interactions between protons, walls and charged monomers. At $z = 0$, the electrostatic potential is known, a condition that serves to represent a conductive wall. In principle, the constant flux of protons at the anode generate an attraction to the charged negative monomers. However, the "proton images" with respect to the wall are negative, thereby pushing them away from the anode[58,59]. The resulting distribution, which balances both interactions: proton-monomer and monomer-wall, drives the presence of the $z \approx 0.8\sigma$ local minima in the proton concentration and the $z \approx 1.6\sigma$ first peak in the sulfonated monomers. The relative position between protons and charged monomers follow the values for the Debye length in Table 1: around 1σ or 2σ. On the other hand, near the cathode at $z = L_z$, the number density of sulfonated monomers is abnormally higher than the uncharged ones. This is a consequence of the $C_+ = 0$ condition at the cathode, which allows charged monomer adsorption. This phenomenon is more significative as the polymer concentration and/or the degree of sulfonation are low. In other words, high values of DS and Φ_P determine the stability of the membrane by decreasing the polymer mobility (diffusion) and forming uniform distributions of protons and charged monomers.

According to our results, DS = 0.3 can be thought of as a critical degree of sulfonation to ensure uniform distributions through the membrane: (i) DS = 0.1 are always non-uniform, and (ii) DS = 0.5 are always uniform. In addition, at DS = 0.3, the controlling variable towards uniformity is the polymer mobility (diffusion): (iii) a concentrated polymer solution, $\Phi_P = 0.4$, the molecules are able to diffuse, move and accommodate near the walls, while (iv) polymer molecules at overlap concentrations or higher, $\Phi_P \geq 0.6$, have a low diffusion and their mobility is highly reduced. Envisioning the high correlation between uniform distributions through the membrane and proton conduction, our results are congruent with previous experimental studies that concluded that SPEEK and Nafion membranes with DS < 0.3 lack ion and proton conduction capability[60–64].

We measured the monomer-to-monomer probability distribution function through a two-dimensional radial distribution function, $g_{xy}(r)$ (where r is the Euclidean distance between

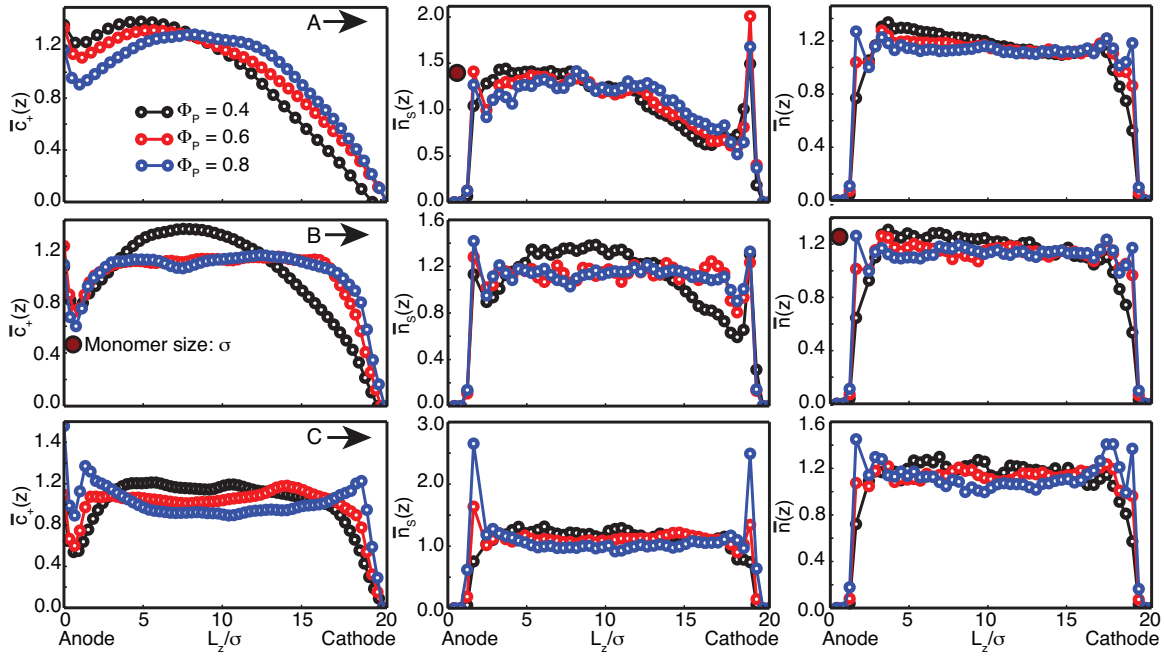

Fig. 2 Time averaged **proton** concentration (left), number density of **sulfonated** monomers (center) and number density of **uncharged** monomers (right) along the $z-$direction for a membrane with $L_z = 5R_G$, $\Phi_P = [0.4, 0.6, 0.8]$ and: **A.** DS = 0.1; **B.** DS = 0.3; and **C.** DS = 0.5.

monomers). In general, we found that the probability of finding the first neighboring monomers at $r = \sigma$ increases with DS. For $\Phi_P \leq 0.6$, the probability depends strongly on DS. For instance, for DS = 0.1 and $\Phi_P = 0.4$, there is a low probability of finding a neighbor: $g_{xy}(\sigma) = 0.5$; while for DS = 0.5 and $\Phi_P = 0.6$, the probability is relatively high: $g_{xy}(\sigma) = 1.4$. On the other hand, for $\Phi_P = 0.8$, there is always a high probability of finding the first monomer neighbor at $r = \sigma$: $g_{xy}(\sigma) \in [1.3, 1.5]$. According to Spohr et al.[65–68], a $g_{xy}(\sigma) > 1$ favors the formation of water clusters that drive polymer segregation and channel conduction. Our result for $\Phi_P = 0.8$, i.e. the presence of monomer neighbors at $r = \sigma$ independent of DS, is consistent with previous reports on SPEEK membranes[12].

3.2 Membrane stability with DS $\geq$ 0.3 and $\Delta\phi \neq 0$

To test the stability of membranes with DS $\geq$ 0.3, we now proceed to apply an electrostatic potential difference between the anode and the cathode. We impose a $\Delta\phi_{\text{cell}} = \phi_A - \phi_C$, by defining $\phi_A = -\Delta\phi_{\text{cell}}/2$ and $\phi_C = +\Delta\phi_{\text{cell}}/2$. A 100 μm SPEEK membrane typically operates with a $\Delta\phi_{\text{cell}} = 0.74$ V[24,69]. We, therefore, adopt a $\Delta\phi_{\text{cell}} = 0.014$ V as the operational potential difference in the $L_z = 5R_G$ membrane. Figures 3, 4 and 5 summarize the time averaged proton concentration and number density of sulfonated (charged) monomers as a function of the $z-$direction for $\Phi_P = 0.4$, 0.6 and 0.8, respectively. We are not including the number density of uncharged monomers because they follow the same rational than the profiles in Fig. 2(right).

The effects of the potential difference in membranes with $\Phi_P =$ 0.4 are shown in Fig. 3. Rigorously, the polymer volume fraction defines this membrane as a concentrated polymer solution. Consequently, as the voltage is increased, the mobility of the polymer chains allows a disruption of the membrane structure. Even for polymers with DS = 0.5, the voltage drives a non-uniform distribution of protons. Noticeable differences are observed in the sulfonated monomer distributions between DS = 0.3 and DS = 0.5. When the polymer charge is DS = 0.3, polymers tend to be absorbed at the cathode, $z = L_z$, whereas at DS = 0.5, the high charge drives a more uniform distribution towards the center of the membrane. Note that as the voltage is increased, the desire of the charged monomers to be close to de cathode also decreases.

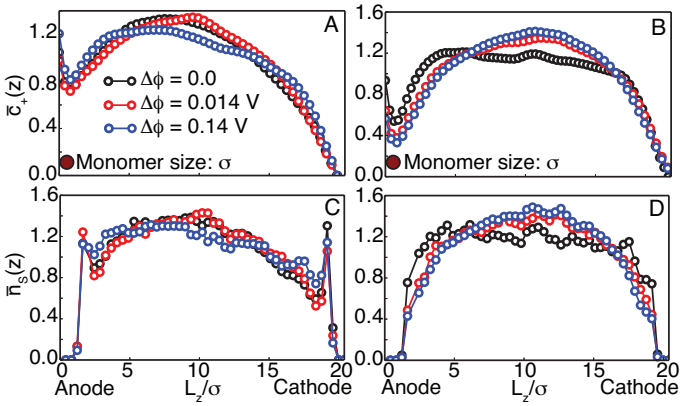

Fig. 3 Time averaged **proton** concentration (top) and number density of **sulfonated** monomers (bottom) the $z-$direction for a membrane with $L_z = 5R_G$, $\Phi_P = 0.4$ and $\Delta\phi = [0.0, 0.014, 0.14]$ V: **A-C.** DS = 0.3; and **B-D.** DS = 0.5

Once the mobility of the chains is drastically reduced, $\Phi_P \geq$ 0.6, the uniformities within the membrane, for protons and monomers, are always conserved. Figures 4 and 5 summarize the proton and charged monomers' distributions along the con-

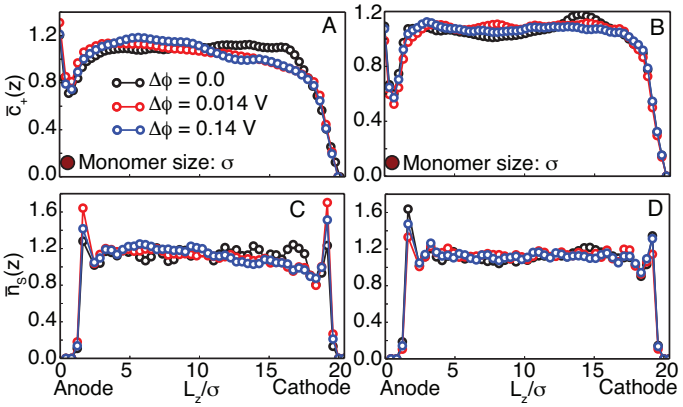

Fig. 4 Time averaged **proton** concentration (top) and number density of **sulfonated** monomers (bottom) the $z-$direction for a membrane with $L_z = 5R_G$, $\Phi_P = 0.6$ and $\Delta\phi = [0.0, 0.014, 0.14]$ V: **A-C.** DS = 0.3; and **B-D.** DS = 0.5

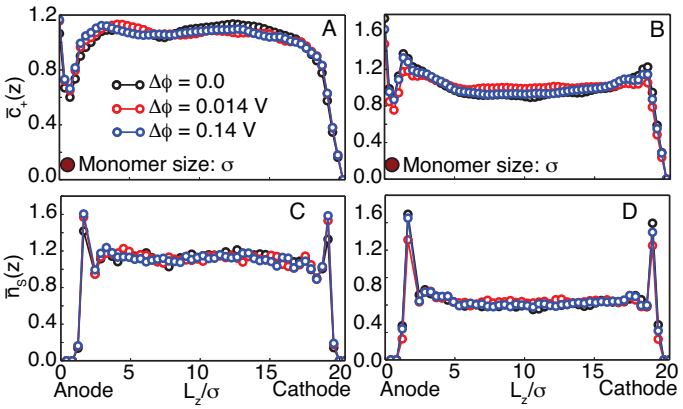

Fig. 5 Time averaged **proton** concentration (top) and number density of **sulfonated** monomers (bottom) the $z-$direction for a membrane with $L_z = 5R_G$, $\Phi_P = 0.8$ and $\Delta\phi = [0.0, 0.014, 0.14]$ V: **A-C.** DS = 0.3; and **B-D.** DS = 0.5

fined direction for different applied voltages. Some general observations are in order: (i) as DS increases, the number density of sulfonated monomers at $z \approx 1.6\sigma$ and $z = L_z - \sigma$ increases, (ii) despite these accumulations that are parallel to the walls, protons and charged monomers are internally uniform, and (iii) the stability of the membrane, quantified by the concentration uniformity, increases as the degree of sulfonation is increased.

It is important to highlight that the concentrations and distributions in Figs. 2 to 4 are time averages, therefore, the uniform distributions are not indications that the membrane is completely immobile. On the contrary, polymer segments, monomers and entire molecules constantly diffuse through the membrane, with a diffusion time that increases as the polymer concentration increases. The high correlation between sulfonated monomers and the proton concentration that we are predicting agrees with previous studies that suggested that the SO_3^- functional groups are responsible for the membrane morphology[70–72].

3.3 Confinement effects: $L_z = 5R_G$ vs. $L_z = 10R_G$

To continue the validation that DS = 0.3 and $\Phi_P \geq 0.6$ are the limiting conditions to guarantee membrane stability and uniformity, we study the effects of the membrane thickness or "polymer confinement". Figure 6 shows the averaged proton concentration and number density of charged monomers for membranes with DS = 0.3 and thicknesses $L_z = 5R_G$ and $L_z = 10R_G$ as a function of the polymer concentration. Below polymer overlap, $\Phi_P = 0.4$, the distributions within the membrane are still not uniform once the confinement is increased; however, there is a clear improvement for the $L_z = 10R_G$ membrane. This tendency of "better distributions as the thickness is increased" is crucial once $\Phi_P \geq 0.6$, where according to Fig. 6, protons and monomers are able to sustain a time-averaged uniformity. At the cathode and anode, the monomers (charged and uncharged) no longer show evidence of parallel packaging layers for $L_z = 10R_G$. For membranes with DS = 0.1 and DS = 0.5 (data not shown), the previously discussed behaviors are enhanced for better and worse: (i) for $\Phi_P < 0.6$ and DS = 0.1, the distributions are less uniform than DS = 0.3, (ii) for $\Phi_P \geq 0.6$ and DS = 0.5, the inner membrane structure is flat uniform.

In Fig. 7, we tested the effects of an electrostatic potential difference between the cathode and anode for membranes with $L_z = 10R_G$ and DS = 0.3. We sustain the same level of electric field by applying a $\Delta\phi = [0.0, 0.028, 0.28]$ V. These results demonstrate, similar to the $L_z = 5R_G$ membrane, that as long as DS ≥ 0.3 and the polymer mobility is highly reduced, above overlap, an electric field is not able to perturb the time-averaged membrane's inner structure.

3.4 Current i, structure factor ψ and conductivity κ

Now that we have established limiting conditions for membrane uniformity (DS ≥ 0.3 and $\Phi_P \geq 0.6$), hinting the proper generation of proton channels to ensure conduction, we proceed to provide quantitative descriptors of the membrane exchange capabilities.

Assuming that the limiting factor for proton conduction is their diffusion from the anode to the cathode, common feature in fuel cells, the current can be estimated by the proton flux: $i = F\mathbf{j}_+$[35,73,74]. Figure 8 shows the current time evolution for three representative cases: (i) a "poor" membrane with $\Phi_P = 0.4$ and DS = 0.1; (ii) a "stable" membrane with $\Phi_P = 0.6$ and DS = 0.3; and (iii) a "rich" membrane with $\Phi_P = 0.8$ and DS = 0.3. At $t = 0$, the proton and monomers are constantly distributed and we only include the current dynamics over 80 μs. According to Fig. 8A, the current in poor membranes decreases to near zero values as the polymer segregation occurs. There is fast initial consumption of protons near the cathode and the absence of charged monomer connectivity avoids the current to be sustained. On the other hand, for stable and rich membranes, Figs. 8B and 8C, the current increases after the initial proton consumption due to the formation of the conduction channels that establish a continuous proton flux from the anode to the cathode. These interconnections, driven by the sulfonated monomers, were also observed and reported in previous works[68,75,76]. In Fig. 8, we are including two dimensional average contours of the proton concentration

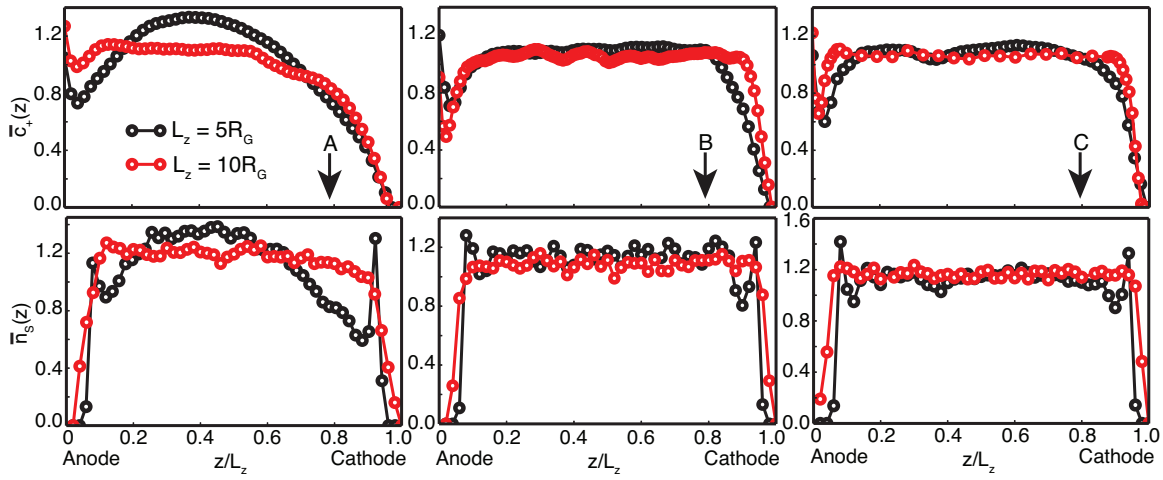

Fig. 6 Time averaged **proton** concentration (top) and number density of **sulfonated** monomers (bottom) the $z-$direction for membranes with $L_z = 5R_G$ and $L_z = 10R_G$. The DS = 0.3 and $\Delta\phi = 0$: **A.** $\Phi_P = 0.4$; **B.** $\Phi_P = 0.6$; and **C.** $\Phi_P = 0.8$.

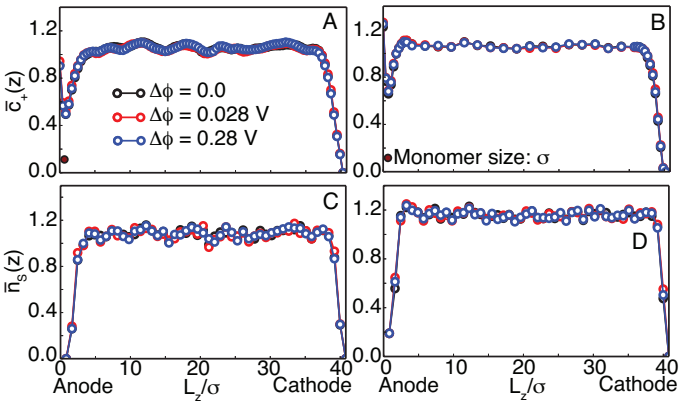

Fig. 7 Time averaged **proton** concentration (top) and number density of **sulfonated** monomers (bottom) the $z-$direction for a membrane with $L_z = 10R_G$, DS = 0.3 and $\Delta\phi = [0.0, 0.028, 0.28]$ V: **A-C.** $\Phi_P = 0.6$; and **B-D.** $\Phi_P = 0.8$

for the three representative cases. The contours suggest that the magnitude of the steady-state current depends on the density of channels or interconnections. Concomitantly, no channels for the poor membrane drive a purely Fickean diffusive proton current of 0.010 A/cm^2, whereas the interconnections for the stable and rich membranes result in 0.155 A/cm^2 and 0.280 A/cm^2, respectively. The higher density of channels demarcates an important difference between a limiting stable membrane, with $\Phi_P = 0.6$ and DS = 0.3, and rich membranes with $\Phi_P > 0.6$ and DS ≥ 0.3. Therefore, the previously discussed uniformity in protons and monomers over time along the membrane is not enough to ensure an effective proton conduction.

A feature to highlight is that our mesoscopic and multi-scale model is able to predict polymer segregation and the formation of proton channels for conduction. The interconnections between the anode and cathode do not depend on specific sulfonated monomer distributions; recall that the sulfunated groups are randomly placed at every polymer molecule that constitutes the membrane. Jang et. al[72] and Savage and Voth[71] used molecular dynamics simulations and reported that the membrane segregation depends strongly on the sulfonic group distribution. We believe that this particular discrepancy between our model and their model is a consequence of the different length scales; their periodic box is between 1.5 to 2.0 nm, while our confined system is in the order of hundreds of nanometers.

The structure factor $\psi(t)$ serves as a parameter that quantifies the segregation in a polymeric membrane for proton exchange[22]. In this work, we define this factor by:

$$\psi(t) = \frac{1}{V}\int\left(\left[\frac{C_+(\mathbf{x},t)}{C_+^0}\right]^2 - 1\right)d\mathbf{x}, \qquad (19)$$

which, in principle, provides a measurement of the level of separation between the hydrophobic and the hydrophilic sections of the polymer[21,22,60,61]. Consequently, a high value of the structure factor is typically associated with a better membrane structure towards an efficient proton conduction. In Figure 9, we are showing the structure factor for two systems: a poor membrane with $\Phi_P = 0.4$ and DS = 0.1 and a rich one with $\Phi_P = 0.8$ and DS = 0.3. What we want to highlight is that even though $\psi_{\text{poor}} \approx 0.5 > \psi_{\text{rich}} \approx 0.3$ there is no connectivity between anode and cathode, resulting in low proton conduction for the poor membrane (as indicated in Fig. 8A). In the figure, we are also including representative iso-surfaces for both membranes. Effectively, there is a higher segregation for the poor case, but the protons are located near the anode and the polymer molecules do not guarantee the connectivity through the membrane. In contrast, the lower separation of domains for the rich membrane ensures an even channel formation and distribution.

With the membrane conductivity κ, we can estimate the proton exchange performance. Considering that in our system the mechanism of conduction is the ionic exchange, the conductivity is calculated as $\kappa = F^2\langle D_+C_+\rangle/RT$. Experimental measurements, of membranes with $0.37 <$ DS < 0.82 at 25 to 80^{o}C, place the value of κ between 1×10^{-3} and 2×10^{-2} S/cm [24,69,77–79]. On the other hand, for hydrogen fed SPEEK membranes, reported values

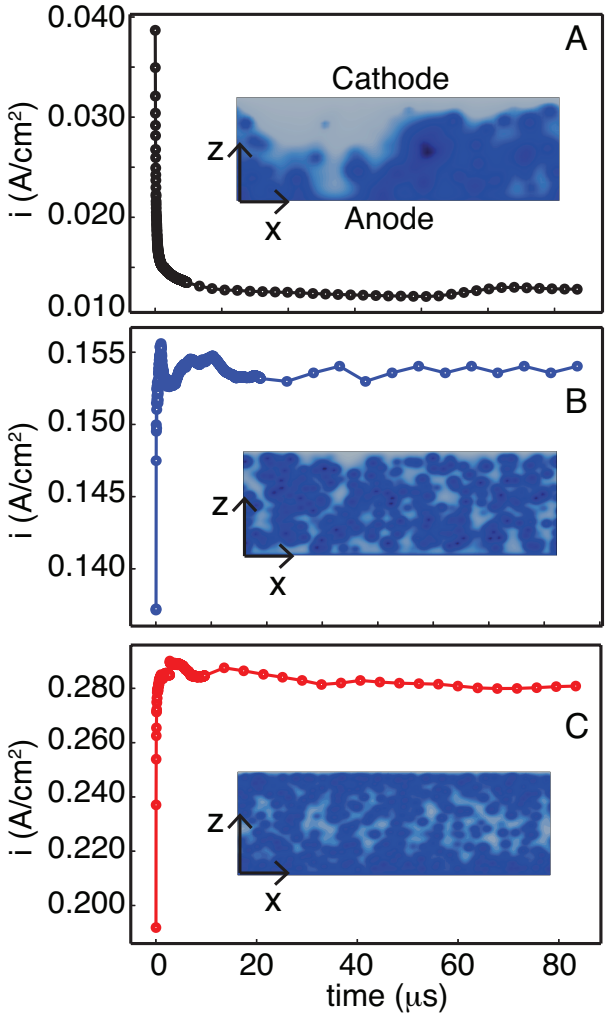

Fig. 8 Current as a function of time for **A.** $\Phi_P = 0.4$ and DS = 0.1; **B.** $\Phi_P = 0.6$ and DS = 0.3 and **C.** $\Phi_P = 0.8$ and DS = 0.3. The inserts are $xz-$planar time-averaged proton concentration contours $\bar{c}_+(x,z)$, where the blue color intensity indicates the low-to-high concentration regions.

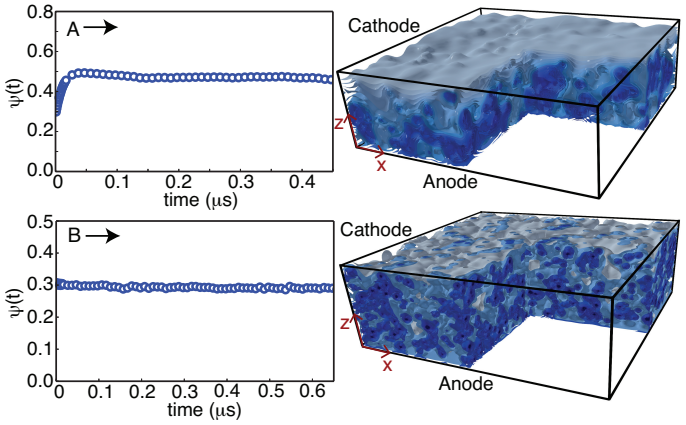

Fig. 9 Structure factor and characteristic proton concentration iso-surfaces for: **A.** $\Phi_P = 0.4$ and DS = 0.1; **B.** $\Phi_P = 0.8$ and DS = 0.3. The blue color intensity, in the iso-surfaces, indicates the low-to-high concentration regions.

for the current are between 25 and 300 mA/cm^2 [80–83]. These experimental values accounted for the detailed complexity of a polymeric membrane for proton exchange: type of catalyzer, fuel, membrane preparation, among others. In our theoretical model, we can hypothesize that all protons that are delivered would react, thereby resulting in a diffusion-controlled membrane. Table 2 summarizes the conductivity, the current and the structure factor for a membrane that is under an experimental potential difference of "$\Delta\phi = 0.7$ V" (meaning that the current is measured for $\Delta\phi = 0.014$ V in the case of $L_z = 5R_G$ and $\Delta\phi = 0.028$ V for $L_z = 10R_G$). The values for the conductivity and structure factor are independent of size and potential gradient, therefore, the values in the table are averages over all the conditions covered by the specific DS and Φ_P.

The importance behind the values in Table 2 is the clear trends that are predicted by the model: (i) the conductivity and current increase monotonically as the polymer concentration and as the degree of sulfonation increase, and (ii) the increasing trend for κ and i as a function of Φ_P is almost linear, while for DS the increase is quadratic, i.e. $[\kappa, i] \sim \Phi_P$ and $[\kappa, i] \sim \mathrm{DS}^2$. In addition, notice that comparing the "stable" (limiting) membrane, with $\Phi_P = 0.6$ and DS = 0.3, against what we denote a "rich" membrane, with $\Phi_P = 0.8$ and DS = 0.5, corroborates previous experimental and theoretical conclusions that suggest the use of membranes with $\Phi_P > 0.7$. Recall that our first tentative conclusion, based on time average proton concentration and monomer number density, was that $\Phi_P = 0.6$ and DS = 0.3 should provide the membrane uniformity intended for conduction. Our scaling laws for $[\kappa, i]$ still place $\Phi_P = 0.6$ and DS = 0.3 as a stable but non-optimum selection, as increasing Φ_P and DS results in a global increase of one order of magnitude in $[\kappa, i]$. Previous experimental studies, on pure SPEEK membranes [69,79,84,85], indicate that degrees of sulfonation higher than 0.5 drives an entire dissolution of the membrane once in contact with water. Consequently, $\Phi_P = 0.8$ and DS = 0.5 offer the best conditions to design and fabricate polymeric membranes for proton exchange with SPEEK.

3.5 Conduction channels for $\Phi_P = 0.8$

In Figure 10, we are illustrating the significant differences in the proton concentration (charged monomers) iso-surfaces for a membrane with $\Phi_P = 0.8$ and the three DS. Our idea is to reinforce the conclusions regarding the level of sulfonation of an optimum SPEEK membrane. The structure factors for DS = 0.1 and DS = 0.3 indicate that there is a level of segregation around 30% and a conductivity increase of one order of magnitude between these sulfonations. However, the separation between hydrophobic and hydrophilic regions is almost 70% for a DS = 0.5, resulting in the highest membrane conductivity. Even though representative, the iso-surfaces in Fig. 10 are able to provide a qualitative picture of the conduction channels: as the DS increases, the structure of the interconnections between the anode and the cathode are well defined and less "diffusive". Consequently, there is a synergistic interplay between the polymer structure, given by the confinement, concentration and entanglements, with the electrostatic-driven diffusion, ensuring a dynamical membrane morphology with a constant presence of proton channels. We

Table 2 Membrane conductivity κ, current i and structure factor $\psi(t\to\infty)$ for "$\Delta\phi = 0.7$ V".

DS ↓	$\Phi_P \rightarrow$	0.4	0.6	0.8
DS = 0.1	κ (S/cm)	$(2.53\pm0.63)\times10^{-4}$	$(4.93\pm1.47)\times10^{-4}$	$(7.04\pm0.52)\times10^{-4}$
at "$\Delta\phi = 0.7$ V"	i (A/cm^2)	$(1.40\pm0.140)\times10^{-2}$	$(2.15\pm0.04)\times10^{-2}$	$(3.35\pm0.01)\times10^{-2}$
	$\psi(t\to\infty)$	0.485 ± 0.06	0.325 ± 0.02	0.365 ± 0.01
DS = 0.3	κ (S/cm)	$(3.07\pm0.49)\times10^{-4}$	$(1.00\pm0.06)\times10^{-3}$	$(2.87\pm0.05)\times10^{-3}$
at "$\Delta\phi = 0.7$ V"	i (A/cm^2)	$(6.40\pm0.92)\times10^{-2}$	$(1.3\pm0.14)\times10^{-1}$	$(2.8\pm0.15)\times10^{-1}$
	$\psi(t\to\infty)$	0.440 ± 0.04	0.315 ± 0.01	0.315 ± 0.02
DS = 0.5	κ (S/cm)	$(2.13\pm0.46)\times10^{-3}$	$(6.58\pm0.48)\times10^{-3}$	$(3.70\pm1.41)\times10^{-2}$
at "$\Delta\phi = 0.7$ V"	i (A/cm^2)	$(9.3\pm0.35)\times10^{-2}$	$(2.8\pm0.56)\times10^{-1}$	$(9.9\pm1.38)\times10^{-1}$
	$\psi(t\to\infty)$	0.295 ± 0.01	0.300 ± 0.01	0.685 ± 0.01

measured the average size of the proton channel from the proton concentration iso-surfaces that go from the anode to the cathode with $C_+ > 3C_+^0$. Based on these criteria, we found that the average size of the channels is between 0.5 and 2 nm, agreeing with previous experimental measurements of poly-sulfonate membranes[86]. In addition, from the 70% segregation, there are, on average, 70% interconnected regions that form proton channels, i.e. 30% of the membrane is proton free, 20% are regions with isolated protons and 50% of the membrane are proton channels.

The bulk polymer diffusion time on water at 25^{o}C is estimated from the molecule radius of gyration and the free draining diffusion coefficient: $\tau_{\text{BULK}} \approx 6\pi\mu R_G^3/k_BT = 2.5$ μs. The level of confinement and concentration that we use to form our polymeric membranes dramatically reduce the polymer diffusivity[23,87–89], thereby increasing the characteristic polymer diffusion time. In Figure 11, we compare the morphology evolution of membranes with DS = 0.1 and DS = 0.5. Here, we also use the proton concentration to illustrate the differences. The level of confinement and concentration are the same for the membranes and the two-dimensional cuts are located in the same position. The time frames are taken every 10 μs, which correspond to four bulk polymer diffusion times. In the figure, we zoomed membrane regions, delimited by the green circles and squares, to show the constant formation and dispersion of the conduction channels, and we use red dotted lines to mark proton paths from the anode to the cathode. We found that for DS = 0.5, the membrane mobility is higher when compared with one with DS = 0.1. This increase in polymer segment diffusion, driven by the electrostatic contributions, is what ensures the dynamic formation of channels. It is essential for a proper proton conduction and it explains the sudden increase in performance for membranes with DS > 0.3.

4 Conclusions

We developed an unprecedented multi-scale mesoscopic model to simulate the conduction channel formation in a poly-sulfonated membrane for proton exchange. Our model explicitly includes the effects of polymer concentration, degree of sulfonation and confinement over length scales over hundreds of nanometers. The polymeric membrane is constructed by freely jointed mesoscopic polymer chains that represent sulfonated poly(ether ether ketone) molecules with randomly distributed sulfonated-charged monomers that obey a specific degree of sulfonation. These molecules are embedded in a continuous solvent containing protons. The multi-scale character of the polymeric membrane is resolved with the Nernst-Planck-General geometry Ewald-like method (NP-GgEm), introduced by Hernández-Ortiz and de Pablo[17], adopting the Green's function formalism for the long-range electrostatic interactions.

We found that a polymer concentration above overlap, $\Phi_P > 0.6$, and a degree of sulfonation DS> 0.3 ensure proton and monomer uniformities through the membrane. This "stable" condition perdures as an electrostatic potential is applied and as the thickness of the membrane is increased. However, the stable conditions ($\Phi_P = 0.6$; DS$= 0.3$) do not ensure the constant or proper formation of proton channels.

Our results correlate with previous experimental efforts, where "rich" polymer conditions were suggested to be necessary for an optimum proton exchange. These are high polymer concentrations with limiting degrees of sulfonation around 50%. Our model explains these conclusions based on the predicted linear proportionality of the membrane conductivity, κ, and current, i, with the polymer concentration and their quadratic dependency on the degree of sulfonation: $[\kappa, i] \sim \Phi_P$ and $[\kappa, i] \sim \text{DS}^2$. We believe that the conductivity and current increase linearly with the polymer concentration because, as the polymer concentration increases, the number of charged monomers increases linearly (for a constant DS). On the other hand, a change in the degree of sulfonation implies a volumetric variation of the charges in the polymer molecules. This increase drives the segregation of the charged monomers, which, consequently, results in a proton desire of inter-connect the membrane domains. However, the membrane is effectively a confined/bi-dimensional system with an exponential screening of the potential along the confined direction. Consequently, the current and conductivity have a quadratic dependance with respect to DS.

We also determined a degree of sulfonation higher than 30% is central to the formation of non-diffusive proton channels. We identified $\Phi_P = 0.8$ and DS = 0.5 as the best conditions to ensure a constant and high membrane conductivity. On average, we found that this membrane has 30% proton free, 20% isolated proton regions and 50% of proton channels. Finally, we found that the proton channels are dynamical and in constant formation/destruction driven by the electrostatic increase of the polymer segment mobility.

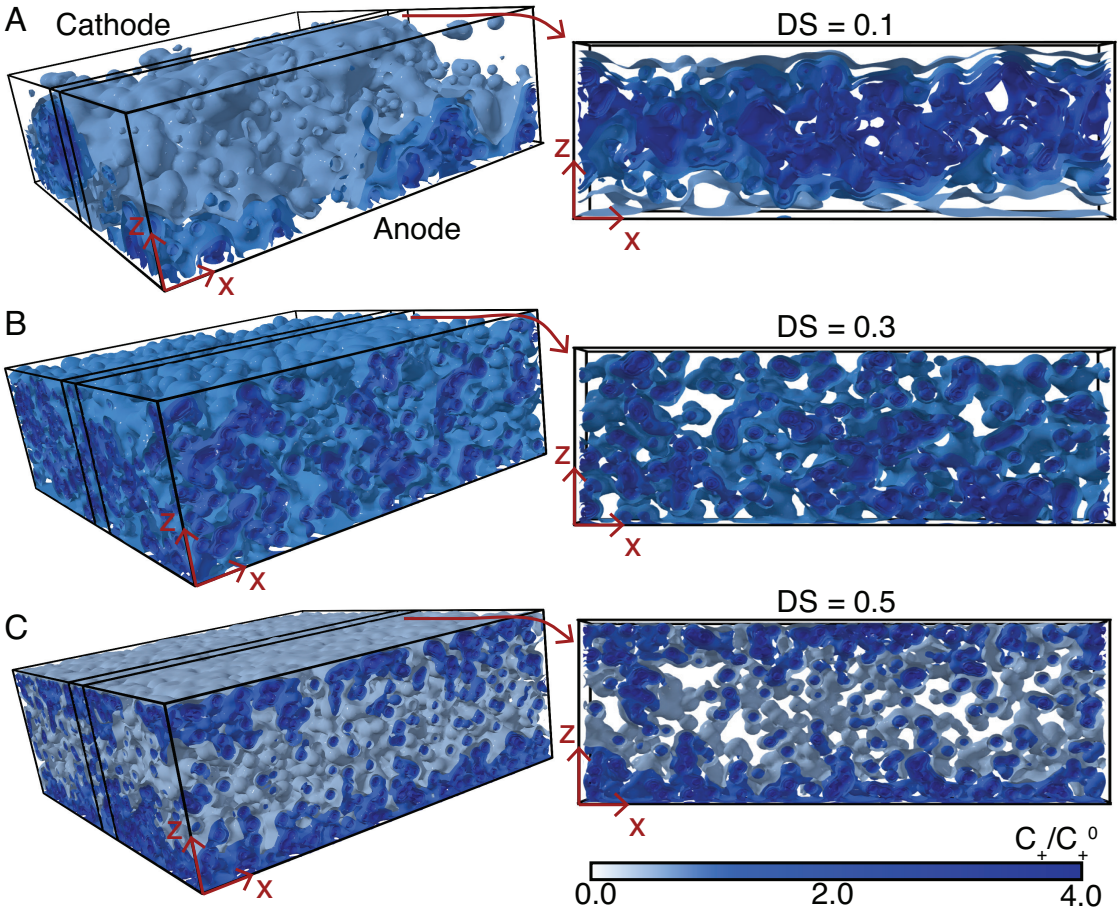

Fig. 10 Three- and two-dimensional proton concentration iso-surfaces for a membrane with $\Phi_P = 0.8$ and: **A.** DS = 0.1; **B.** DS = 0.3; and **C.** DS = 0.5. The blue color intensity indicates the low-to-high concentration regions and the color map is constant for the three cases.

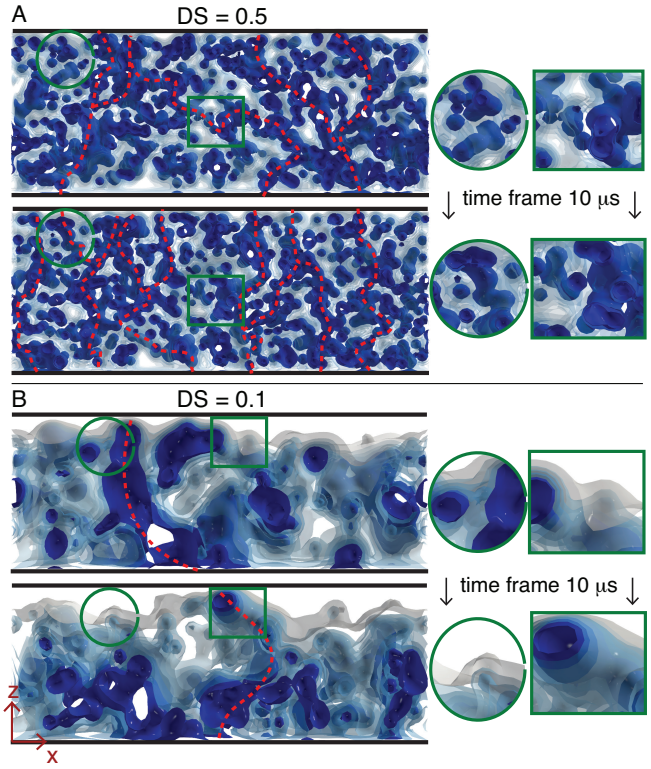

Fig. 11 Time evolution of proton concentration iso-surfaces for $\Phi_P = 0.8$ and membranes with DS = 0.1 and DS = 0.5. The time frames are taken every 10 μs. The blue color intensity indicates the low-to-high proton concentration. The green circles and squares highlight the proton (polymer) mobility between timeframes. The conduction channels are calculated from adjacent and continuum sections that have a proton concentration $C_+ > 3C_+^0$.

Conflicts of interest

The authors have no conflicts of interest to declare.

Acknowledgements

This work was partially supported by Colciencias through the "National Ph.D. Program" and it is part of the Colombia/Wisconsin One-Health Consortium at the Universidad Nacional de Colombia–Medellín. At the University of Chicago, support was given by "MICCoM", as part of the Computational Materials Sciences Program funded by the U.S. Department of Energy, Office of Science, Basic Energy Sciences, Materials Sciences and Engineering Division and by the U.S. Department of Energy, Office of Science, Advanced Scientific Computing Research, under Contract DE-AC02-06CH11357. We gratefully acknowledge the computing resources provided on Blues and Fusion, high-performance computing clusters operated by the Laboratory Computing Resource Center at Argonne National Laboratory.

5 Appendix

5.1 Global field numerical approach

The solution for the global contribution of the electrostatic potential starts by translating the charge of the discrete particles to a fluid mesh. This global density is defined as follows

$$\rho_g(\mathbf{x}_m) = F\sum_{i=1}^{n_I} z_i C_i(\mathbf{x}_m) + \frac{\xi^3 e}{\pi^{3/2}}\sum_{\nu=1}^{n_p} z_\nu \exp(-\xi^3 \parallel \mathbf{x}_\nu - \mathbf{x}_m \parallel^2), \tag{20}$$

where $\rho_g(\mathbf{x}_m)$ is the global charge density in each node of the mesh with coordinates $\mathbf{x}_m$. This "discretized" global charge density is used to solve Poisson's equation for the global electrostatic field at the fluid mesh. In this paper, we used a Fast Fourier Transform (FFT)[90,91] method for the periodic directions (x and y), while a second order finite difference method (FDM)[92] in the confined direction (z), i.e.

$$-\tilde{\phi}_g(k_x,k_y,z_{m-1}) + [2+(\Delta z)^2(k_x^2+k_y^2)]\tilde{\phi}_g(k_x,k_y,z_m) - \tilde{\phi}_g(k_x,k_y,z_{m+1}) = \frac{-\tilde{\rho}_g(k_x,k_y,z_m)}{\varepsilon\varepsilon_0}(\Delta z)^2, \tag{21}$$

where $\tilde{\phi}_g(k_x,k_y,z_m)$ and $\tilde{\rho}_g(k_x,k_y,z_m)$ are the k_x and k_y Fourier modes of the global electrostatic potential and charge density at node m, respectively. Each point of the mesh is located at $\mathbf{x}_m = (x_m, y_m, z_m)$. Equation (21) results in a tri-diagonal system for the 1D-FDM discretization in the $z-$direction for every (k_x,k_y) Fourier mode. Thomas algorithm is used to solve the system[93].

5.2 Nernst-Planck numerical approach

For the numerical solution and evolution of the Nernst-Planck equation, the same fluid mesh form the Poisson's equation is used. Consequently, the mesh resolution must be selected appropriately to resolve the fluid characteristic length and time scales. The Nernst-Planck equation is evolved using a semi-implicit Euler time integration scheme, where the Crank-Nicolson method is employed for the concentration laplacian operator and the nonlinear terms are considered explicitly[92]:

$$\left[C_i(x,y,z) - \frac{D_i\Delta t}{2}\nabla^2 C_i(x,y,z)\right]^{t+\Delta t} = [B_i(x,y,z)]^t, \tag{22}$$

where

$$[B_i(x,y,z)]^t = \left[C_i(x,y,z) + \frac{D_i\Delta t}{2}\nabla^2 C_i(x,y,z) + \frac{ez_iD_i\Delta t}{k_bT}\{\nabla C_i(x,y,z)\cdot\nabla\phi(x,y,z) + \right. \tag{23}$$

$$\left. C_i(x,y,z)\nabla^2\phi(x,y,z)\}\right]^t. \tag{24}$$

For the spacial operators, we followed use a FFT in the periodic directions and a 2nd order FDM in the confined direction, i.e.

$$\left[-\tilde{C}_i(k_x,k_y,z_{m-1}) + \Theta(k_x,k_y)\tilde{C}_i(k_x,k_y,z_m) - \tilde{C}_i(k_x,k_y,z_{m+1})\right]^{t+\Delta t} = \left(\frac{2\Delta z^2}{D_i\Delta t}\right)\left[\tilde{B}_i(k_x,k_y,z_m)\right]^t, \tag{25}$$

where

$$\Theta(k_x,k_y)=\left(\frac{2\Delta z^2}{D_i\Delta t}\right)\left[1+D_i\Delta t(k_x^2+k_y^2+\frac{1}{\Delta z^2})\right]. \qquad (26)$$

Similar to the global electrostatic potential solution, the resulting scheme is a tri-diagonal matrix system that is also resolved by the Thomas algorithm.

References

1 T. Harit and F. Malek, *Separation and Purification Technology*, 2017, **188**, 394 – 398.

2 D. Zioui, O. Arous, N. Mameri, H. Kerdjoudj, M. S. Sebastian, J. Vilas, J. Nunes-Pereira and S. Lanceros-MÃĺndez, *Journal of Hazardous Materials*, 2017, **336**, 188 – 194.

3 D. Wang, J. Hu, D. Liu, Q. Chen and J. Li, *Journal of Membrane Science*, 2017, **524**, 205 – 213.

4 X.-M. Zhang, Z.-H. Tu, H. Li, L. Li, Y.-T. Wu and X.-B. Hu, *Journal of Membrane Science*, 2017, **527**, 60 – 67.

5 F. M. Ashcroft, *Ion Channels and Disease*, Academic Press, 1999.

6 P. Pei, Y. Li, H. Xu and Z. Wu, *Applied Energy*, 2016, **173**, 366–385.

7 D. Cheddie and N. Munroe, *Journal of Power Sources*, 2005, **147**, 72–84.

8 R. Sousa and E. R. Gonzalez, *Journal of Power Sources*, 2005, **147**, 32–45.

9 E. O. Johansson, T. Yamada, B. Sundén and J. Yuan, *International Journal of Hydrogen Energy*, 2015, **40**, 1800–1808.

10 W. Goddard, B. Merinov, A. Van Duin, T. Jacob, M. Blanco, V. Molinero, S. S. Jang and Y. H. Jang, *Molecular Simulation*, 2006, **32**, 251–268.

11 E. Spohr, *Journal of Molecular Liquids*, 2007, **136**, 288–293.

12 A.-T. Kuo, W. Shinoda and S. Okazaki, *The Journal of Physical Chemistry C*, 2016, 25832Ð25842.

13 J. T. Wescott, Y. Qi, L. Subramanian and T. Weston Capehart, *Journal of Chemical Physics*, 2006, **124**, 1–14.

14 B. Kirby, *Micro- and Nanoscale Fluid Mechanics: Transport in Microfluidic Devices*, Cambridge University Press, Cambridge, 2010.

15 K. Binder, *Monte Carlo and Molecular Dymanics Simulations in Polymers Science*, Oxford University Press, Oxford, 2008, vol. 20, p. 356.

16 T. Cosgrove, *Colloid Science: Principles, Methods and Applications*, Wiley-Blackwell, West Sussex, London, 2nd edn, 2010, pp. 1–288.

17 J. Hernandez-Ortiz and J. de Pablo, *J Chem Phys*, 2015, **143**, 014108.

18 J. P. Hernández-Ortiz, J. J. De Pablo and M. D. Graham, *Physical Review Letters*, 2007, **98**, 1–4.

19 M. T. Bishop, F. E. Karasz, P. S. Russo and K. H. Langley, *Macromolecules*, 1985, **18**, 86–93.

20 I. N. Veselov and P. V. Komarov, *Nanotechnologies in Russia*, 2011, **6**, 476–482.

21 P. Komarov, I. Veselov, P. Chu, P. Khalatur and a.R. Khokhlov, *Chemical Physics Letters*, 2010, **487**, 291–296.

22 P. V. Komarov, I. N. Veselov, P. P. Chu and P. G. Khalatur, *Soft Matter*, 2010, **6**, 3939.

23 R. Bird, C. Curtiss, R. Armstrong and O. Hassager, *Dynamics of Polymer Liquids: Kinetic Theory*, John Wiley & Sons, New York, 2nd edn, 1987, vol. 2.

24 M. M. Norddin, A. Ismail, D. Rana, T. Matsuura, A. Mustafa and A. Tabe-Mohammadi, *Journal of Membrane Science*, 2008, **323**, 404–413.

25 D. Allen M. & Tildesley, *Computer Simulation of Liquids*, Oxford Science Publications, 1987.

26 D. Frenkel and B. Smith, *Understanding Molecular Simulations-From Algorithms to Applications*, Academic Press, San Diego, 1996.

27 *Electrical Phenomena at Interfaces and Biointerfaces*, ed. H. Ohshima, John Wiley & Sons, New Jersey, 2012.

28 H. Ohshima, *Advances in Colloid and Interface Science*, 1994, **53**, 77–102.

29 H. Ohshima, T. W. Healy and L. R. White, *Journal Of Colloid And Interface Science*, 1982, **90**, 17–26.

30 H.-C. Öttinger, *Stochastic Processes in Polymeric Fluids*, Springer, Berlin, 1996.

31 H. Risken and T. Frank, *The Fokker-Planck Equation: Methods of Solutions and Applications (Springer Series in Synergetics)*, Springer, 1996.

32 H. Power and L. C. Wrobel, *Boundary Integral Methods in Fluid Mechanics*, Computational Mechanics Publications, Southampton, 1995.

33 J. P. Hernández-Ortiz, M. Chopra, S. Geier and J. J. De Pablo, *Journal of Chemical Physics*, 2009, **131**, 1–8.

34 J. F. Brady and G. Bossis, *Annual Review Of Fluid Mechanics, Vol 43*, 1988, **20**, 111–157.

35 W. Deen, *Analysis of Transport Phenomena*, Oxford University Press, Oxford, 1998.

36 E. L. Cussler, *Diffusion: Mass Transfer in Fluid Systems*, Cambridge University Press, Cambridge, 2nd edn, 1997.

37 A. J. Easteal, W. E. Price and L. A. Woolf, *Furuday Trans. I*, 1989, **85**, 1091–1097.

38 S. H. Lee and J. C. Rasaiah, *Journal of Chemical Physics*, 2011, **135**, 124505.

39 P. P. Ewald, *Ann. Phys.*, 1921, **369**, 253–287.

40 M. Deserno and C. Holm, *J. Chem. Phys.*, 1998, **109**, 7678.

41 M. Deserno and C. Holm, *J. Chem. Phys.*, 1998, **109**, 7694.

42 U. Essmann, L. Perera and M. Berkowitz, *J. Chem. Phys.*, 1995, **103**, 8577.

43 D. van der Spoel, E. Lindahl, B. Hess, G. Groenhof, A. E. Mark and H. J. C. Berendsen, *Journal of Computational Chemistry*, 2005, **26**, 1701–1718.

44 E. Lindahl, B. Hess and D. van der Spoel, *Journal of Molecular Modeling*, 2001, **7**, 306–317.

45 S. Plimpton, *J Comp Phys*, 1995, **117**, 1–19.

46 P. Pranay, S. G. Anekal, J. P. Hernandez-Ortiz and M. D. Graham, *Phys. Fluids*, 2010, **22**, 123103.

47 P. Pranay, R. G. Henríquez-Rivera and M. D. Graham, *Physics*

Of Fluids, 2012, **24**, 061902.
48 C. Miller, J. P. Hernández-Ortiz, N. L. Abbott, S. H. Gelman and J. J. de Pablo, *Journal of Chemical Physics*, 2008, **129**, 015102.
49 J. P. Hernández-Ortiz, M. Chopra, S. Geier and J. de Pablo, *J. Chem. Phys.*, 2009, **131**, 044904.
50 X. Zhao, J. Li, X. Jiang, D. Karpeev, O. Heinonen, B. Smith, J. P. Hernández-Ortíz and J. J. de Pablo, *The Journal of Chemical Physics*, 2017, **146**, 244114.
51 K. L. Kounovsky-Shafer, J. P. Hernández-Ortiz, K. Jo, T. Odijk, J. J. de Pablo and D. C. Schwartz, *Macromolecules*, 2013, **46**, 8356–8368.
52 K. L. Kounovsky-Shafer, J. P. Hernández-Ortíz, K. Potamousis, G. Tsvid, M. Place, P. Ravindran, K. Jo, S. Zhou, T. Odijk, J. J. de Pablo and D. C. Schwartz, *P. Natl. Acad. Sci. USA*, 2017, **114**, 13400Ð–13405.
53 J. P. Hernández-Ortiz, P. T. Underhill and M. D. Graham, *J. Phys. Condensed Matter*, 2009, **21**, 204107.
54 D. Ausserre, H. Hervet and F. Rondelez, *Macromolecules*, 1986, **19**, 85.
55 J. P. Hernández-Ortiz, H. Ma, J. J. D. Pablo and M. D. Graham, *Korea-Aust Rheol J*, 2008, **20**, 143–152.
56 J. W. Swan and J. F. Brady, *Physics of Fluids*, 2010, **22**, 103301.
57 J. W. Swan and J. F. Brady, *Phys. Fluids*, 2007, **19**, 113306.
58 J. N. Israelachvili, *Intermolecular and Surface Forces*, Academic Press, New York, 1985.
59 R. P. Feynman, R. Leighton and M. Sands, *The Feynman Lectures of Physics*, Addison-Wesley Pub., New York, 1963.
60 W. Y. Hsu, J. R. Barkley and P. Meakin, *Macromolecules*, 1980, **13**, 198–200.
61 W. Y. Hsu and T. D. Gierke, *Journal of Membrane Science*, 1983, **13**, 307–326.
62 Z. Peng, P. Huguet, S. Deabate, A. Morin and A. K. Sutor, *Journal of Raman Spectroscopy*, 2013, **44**, 321–328.
63 S. Deabate, P. Huguet, A. Morin, G. Gebel, Y. Lanteri, Z. Peng and A. K. Sutor, *Fuel Cells*, 2014, **14**, 677–693.
64 B. Bauer, D. J. Jones, J. Rozière, L. Tchicaya, G. Alberti, M. Casciola, L. Massinelli, A. Peraio, S. Besse and E. Ramunni, *Journal of New Materials for Electrochemical Systems*, 2000, **3**, 93–98.
65 E. Spohr, *Journal of Molecular Liquids*, 2007, **136**, 288–293.
66 S. Dokmaisrijan, E. Spohr and S. D. E. Spohr, *Journal of Molecular Liquids*, 2006, **129**, 92–100.
67 E. Spohr, P. Commer and A. A. Kornyshev, *Structure*, 2002, 10560–10569.
68 E. Spohr, *J Computer-Aided Mater Des*, 2008, **14**, 253–258.
69 D. Sangeetha, *International Journal of Polymeric Materials*, 2007, **56**, 535–548.
70 M. E. Selvan, E. Calvo-Muñoz and D. J. Keffer, *The journal of Physical Chemistry B*, 2011, **115**, 3052–61.
71 J. Savage and G. A. Voth, *Journal of Physical Chemistry C*, 2016, **120**, 3176–3186.
72 S. S. Jang, V. Molinero, C. Tahir and G. I. William A., *J. Phys. Chem. B*, 2004, **108**, 3149–3157.
73 F. N. Buchi and G. G. Scherer, *Journal of The Electrochemical Society*, 2001, **148**, A183.
74 S. Koter, W. Kujawski and I. Koter, *Journal of Membrane Science*, 2007, **297**, 226–235.
75 G. Dorenbos and Y. Suga, *Journal of Membrane Science*, 2009, **330**, 5–20.
76 K. D. Kreuer, *Journal of Membrane Science*, 2001, **185**, 29–39.
77 P. Xing, G. P. Robertson, M. D. Guiver, S. D. Mikhailenko, K. Wang and S. Kaliaguine, *Journal of Membrane Science*, 2004, **229**, 95–106.
78 N. P. Berezina and E. N. Komkova, *Colloid Journal*, 2003, **65**, 1–10.
79 L. Li, J. Zhang and Y. Wang, *Journal of Membrane Science*, 2003, **226**, 159–167.
80 V. Neburchilov, J. Martin, H. Wang and J. Zhang, *Journal of Power Sources*, 2007, **169**, 221–238.
81 E. Sengul, H. Erdener, R. G. Akay, H. Yucel, N. Bac and I. Eroglu, *International Journal of Hydrogen Energy*, 2008, **34**, 4645–4652.
82 B. Mecheri, E. Traversa and S. Licoccia, *Journal of Power Sources*, 2008, **178**, 554–560.
83 S. Ren, G. Sun, C. Li, Z. Wu, W. Jin, W. Chen, Q. Xin and X. Yang, *Materials Letters*, 2006, **60**, 44–47.
84 Q. Li, R. He, J. O. Jensen and N. J. Bjerrum, *Chem. Mater*, 2008, **15**, 4896–4915.
85 S. Banerjee and K. K. Kar, *Polymer*, 2017, **109**, 176–186.
86 K. Schmidt-Rohr and Q. Chen, *Nature materials*, 2008, **7**, 75–83.
87 R. M. Jendrejack, J. J. de Pablo and M. D. Graham, *J. Chem. Phys.*, 2002, **116**, 7752–7759.
88 R. M. Jendrejack, M. D. Graham and J. J. de Pablo, *J. Chem. Phys.*, 2000, **113**, 2894.
89 Y.-L. Chen, M. D. Graham, J. J. de Pablo, G. C. Randall, M. Gupta and P. S. Doyle, *Phys. Rev. E*, 2004, **70**, 060901(R).
90 M. Frigo and S. Johnson, Proc. 1998 IEEE Intl. Conf. Acoustics Speech and Signal Processing, 1998, pp. 1381–1384.
91 M. Frigo and S. Johnson, *Proc. IEEE*, 2005, **93**, 216–231.
92 T. A. Osswald and J. P. Hernández-Ortiz, *Polymer Processing: Modeling and Simulation*, Carl Hanser-Verlag, Munich, 2006.
93 W. H. Press, S. A. Teukolsky, W. T. Vetterling and B. P. Flannery, *Numerical Recipes in Fortran 77*, Cambridge University Press, Cambridge, 2nd edn, 1992.